Physics Open 18 (2024) 100202

Contents lists available at ScienceDirect

Physics Open

journal homepage: www.sciencedirect.com/journal/physics-open

Space-temporal structure of the thunderstorm ground enhancements (TGEs)

A. Chilingarian *, D. Pokhsraryan, F. Zagumennov, M. Zazyan

A I Alikhanyan National Laboratory, Yerevan, 0036, Armenia

A B S T R A C T

We analyzed the structure of the Thunderstorm Ground Enhancement (TGE) using a particle detector network on Aragats. We performed a statistical analysis of the particle arrival time series on a nanosecond time scale using the largest TGE event on record, which occurred on May 23, 2023. Our findings confirm that the TGE is a mixture of multiple runaway electron avalanches that arrive independently and provide stable particle flux. The electron accelerator, operated by the dipole that emerges in the lower part of the thundercloud, sends copious electrons and gamma rays toward the Earth's surface that sustains for minutes. The experimental results are supported by simulations of electron multiplication and acceleration in strong atmospheric electric fields. We compare TGEs and Terrestrial Gamma Flashes (TGFs), which are brief bursts observed by gamma-ray detectors in orbit and are thought to be associated with atmospheric discharges.

1. Introduction

Observation of intense particle fluxes on Earth's surface, known as TGEs [1,2], and detection of terrestrial gamma flashes (TGFs) from strong equatorial thunderstorms by orbiting gamma-ray detectors [3] have led to the emergence of a new field of high-energy physics in the atmosphere (HEPA). Relativistic runaway electron avalanche (RREA [4–7]) generates TGEs in the lower atmosphere, while in tropical and subtropical areas at altitudes 10–20 km, it generates TGFs. TGFs consist of the most energetic bremsstrahlung gamma rays, which are detected by fast-moving detectors located 400–600 km from the radiation source. TGEs consist of millions of electrons, gamma rays, and rarely neutrons, covering many km^2 on the Earth's surface and km^3 in the lower atmosphere. Simulations of the electron flux traversal in the strong atmospheric field revealed electrons' copious multiplication and acceleration, forming RREAs, which reached the Earth's surface and ended up as TGEs. Acceleration and multiplication of free atmospheric electrons become possible if the intracloud electric field is larger than the critical value, specific for the particular air density [8–10]. A vast amount of fully described TGE events are available from the Mendeley datasets [11,12] and the database of the Cosmic Ray Division of Yerevan Physics Institute [13]. Developing in the thunderous atmosphere, RREAs form a prolonged (sometimes up to a few 10 min) flux of electrons and gamma rays. Thus, besides the 10–100 kA current of eV energy electrons (lightning stroke), there exists a minutes-long ionizing current of the MeV electrons in the atmosphere. A lightning flash usually terminates this current [14] at different stages of the TGE development. Thus, RREA precedes the lightning flash, possibly guiding the path of a lightning leader [15].

The RREA current is generated by discrete avalanches initiated by a seed electron entering the atmospheric electric field. We call these avalanches extensive cloud showers (ECSs) [16]; Alex Gurevich called them "microbursts" [17]. However, it is unclear how these numerous avalanches are integrated into the TGE flux measured by the surface detectors. The first attempt to estimate the space-temporal structure of RREA was done on Aragats by registering enhancement of the MAKET surface array triggers [2]. Analyzing the TGEs registered on Aragats on 19 September 2009 and 4 October 2010 [2,16], we demonstrated that TGE particles are more or less uniformly distributed within the TGE duration at the area of ≈1000 m^2. To get further insight into the RREA space-time distribution, we performed a new experiment analyzing TGE particles' arrival on the nanosecond time scale over an area of ≈50,000 m^2. Using a fast-synchronized data acquisition system (FSDAQ, [18]), we revealed the TGE space-time structure by detecting avalanche particles' arrival with scintillators directly attached to high-speed oscilloscopes.

2. Method

The TGE detection system consists of 18 plastic scintillators, each with an area of 1 m^2 and thicknesses of 1 and 3 cm. The scintillators were commissioned by the High-Energy Physics Institute in Protvino [19]. Twelve of these scintillators are part of the STAND1 network, located across the Aragats station, covering an area of ≈50,000 m^2. Three

* Corresponding author.
E-mail address: chili@aragats.am (A. Chilingarian).

https://doi.org/10.1016/j.physo.2023.100202
Received 17 October 2023; Received in revised form 12 December 2023; Accepted 14 December 2023
Available online 19 December 2023

identical units of the STAND1 network are located near three main experimental halls – MAKET, SKL, and GAMMA, see Fig. 1a. 1-cm thick scintillators are stacked vertically, and one 3-cm thick plastic scintillator stands apart; see Fig. 1b and c. STAND1 detector has been in operation for ten years, registering spatial distribution of more than 300 TGE at millisecond time scales. The light from the scintillator through optical spectrum-shifter fibers is passed to the photomultiplier FEU-115 M. The maximum luminescence is emitted at the 420-nm wavelength, with a luminescence time of about 2.3 ns. The STAND1 detector is tuned by changing the high voltage applied to the PMT and setting the thresholds for the discriminator shaper. The discrimination level is chosen to guarantee high signal detection efficiency and maximal suppression of photomultiplier noise. The efficiency of scintillators reaches 90 % and more for electron energies above 10 MeV and 2 % for gamma rays with energies above 2 MeV (for the upper scintillators). The energy threshold of the upper scintillators is 0.7–0.8 MeV, and dead time is ∼ 0.7 μs A 50 μs time series of STAND1 detectors, synchronized with NSEF measurements and meteorological parameters, are transferred to the Cosmic ray Division (CRD) database and are available online in graphical and numerical format via the Advanced Data Extraction Infrastructure (ADEI) platform [20].

Four 1 cm thick and one 3 cm thick scintillators are attached to four-channel (Picoscope 6403D) and two-channel (Picoscope 5244B) oscilloscopes (see Fig. 2 for 4-channel Picoscope 6403D, located in the SKL experimental hall). In the MAKET experimental hall, the 3-cm thick scintillator was attached to the 2-channel oscilloscope. The record length of both oscilloscopes was 200 ms, and the sampling rate of signals is 250 MS/s and 156.25 MS/s, corresponding to the sampling intervals of 4 ns and 6.4 ns. The typical duration (full width on half maximum, FWHM) of individual pulses from the scintillators is 20–30 ns. Thus, usually, the signal occupied several sampling intervals. One scintillator, attached to the National Instruments (NI) MyRIO board, registers the 1-s count rate. If the count rate of the 1-s time series exceeded the prechosen limit (usually set to 50 % larger than the average count rate), the MyRio board produced the trigger for the oscilloscope, see Fig. 2. The oscilloscope's trigger-out (synchro) pulse was relayed to the board, which produced the GPS time stamp of the record. This feature enables accurate time synchronization, with time stamps estimated to have an absolute accuracy of tens of nanoseconds. A detailed description of an FSDAQ based on the NI MyRIO board can be found in Ref. [21].

Fig. 3 displays a photo of the CUBE detector deployed in the SKL hall. The CUBE detector was initially comprised of stacked 20 cm thick and 0.25 m^2 area plastic scintillators surrounded by all sides with 1 cm thick plastic scintillators. The main goal of the detector was gamma ray spectroscopy and estimation of the electron-to-gamma ray ratio during TGEs. In 2019, we dismounted the side and bottom detectors and put the upper (veto) scintillator directly above the 20 cm thick scintillators. Thus, the main functions of CUBE scintillators remain, and new experiments with CUBE scintillators and digital oscilloscopes started. We maintain these measurements using the CUBE 1 as a veto scintillator to reject the charged flux (the neutral flux is registered by 20 cm thick spectrometric scintillators below it).

Additionally, electronics permanently keep track of the signal amplitudes from CUBE detectors 2, 3, and 6. These detectors are triggered when large TGEs are detected at Aragats station. CUBE's N 1 scintillator's 1-min count rate was also used to calibrate the flux measured by the 2, 3, and 6 CUBE scintillators.

3. TGE occurred on 23 May 2013

During the last decade, particle detectors on Mt. Aragats in Armenia, Mt. Lomnicky Stit in Slovakia, Mt. Musala in Bulgaria, and now also at Mt. Zugspitze in Germany registered nearly a thousand TGEs [22,23]. Particle flux enhancement on Aragats usually counts 10–20 %, rarely over 100 %. Most TGEs and all large ones occurred in Spring and Autumn (≈80 %) when the outside temperature is in the -2C° - +2C° range and clouds are very low above the Aragats research station (yellow and green colors on the histogram of Fig. 4). Approximately 12 % of TGE events occurred in Summer (red color) and ≈8 % in Winter (brown color). The standard mechanism of cloud electrification involves warm air updrafts that lead to the collisional charging of hydrometeors. This process causes charge separation, resulting in the emergence of lower dipole accelerated electrons downward. When the intracloud electric field exceeds the runaway threshold strength, an RREA process initiates

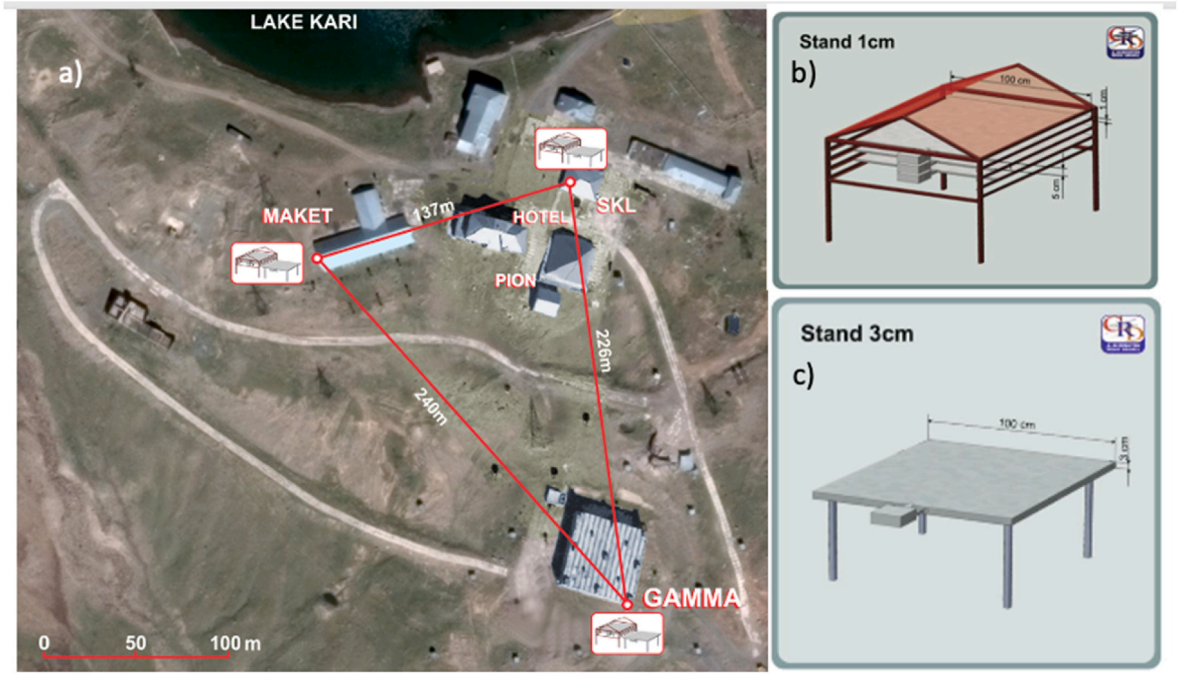

Fig. 1. a) The map of Aragats station with STAND1 network; b) Stand1 unit: vertically stacked 1 cm thick and 1 m^2 area plastic scintillators; c) Stand1 unit: standalone 3 cm thick plastic scintillator with the same area.

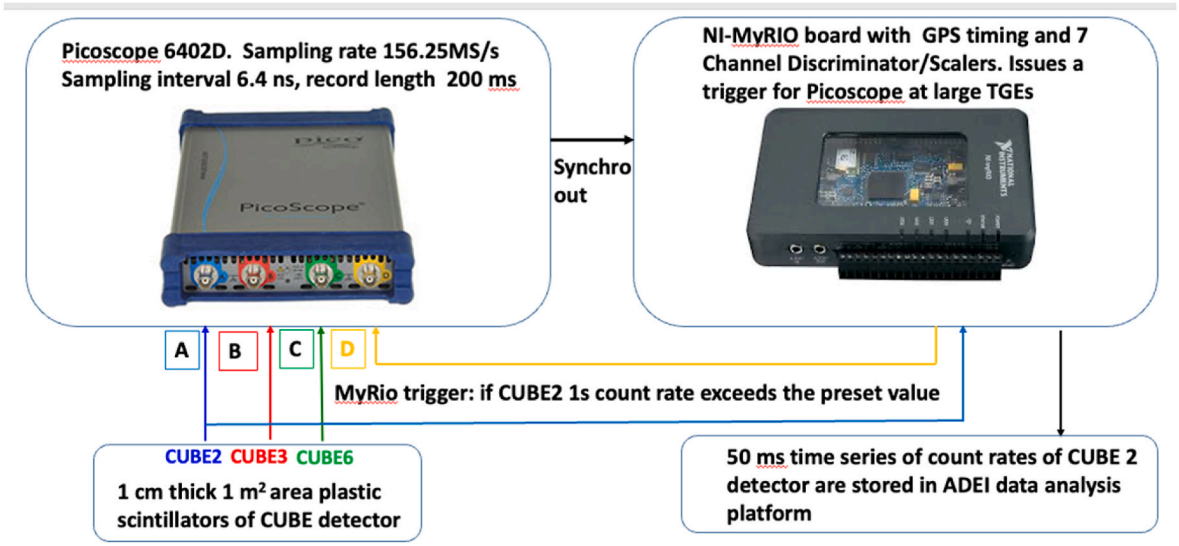

Fig. 2. Block diagram of the FSDAQ located in the SKL experimental hall, a similar system operates in MAKET hall (two-channel Picoscope 5244B.

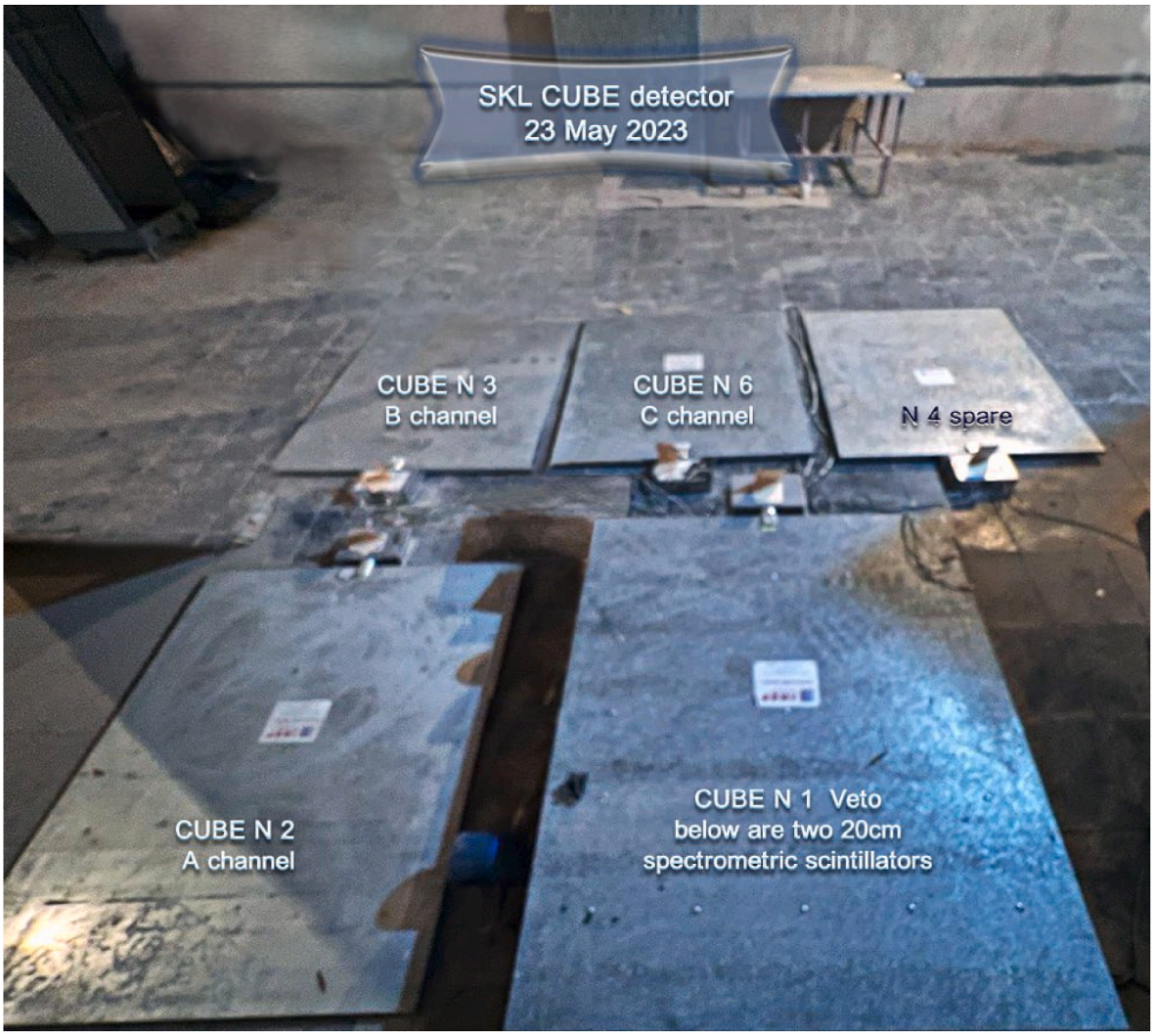

Fig. 3. The CUBE detector's scintillators in the SKL experimental hall beneath a 1 cm wooden roof covered by 7 mm iron tiles.

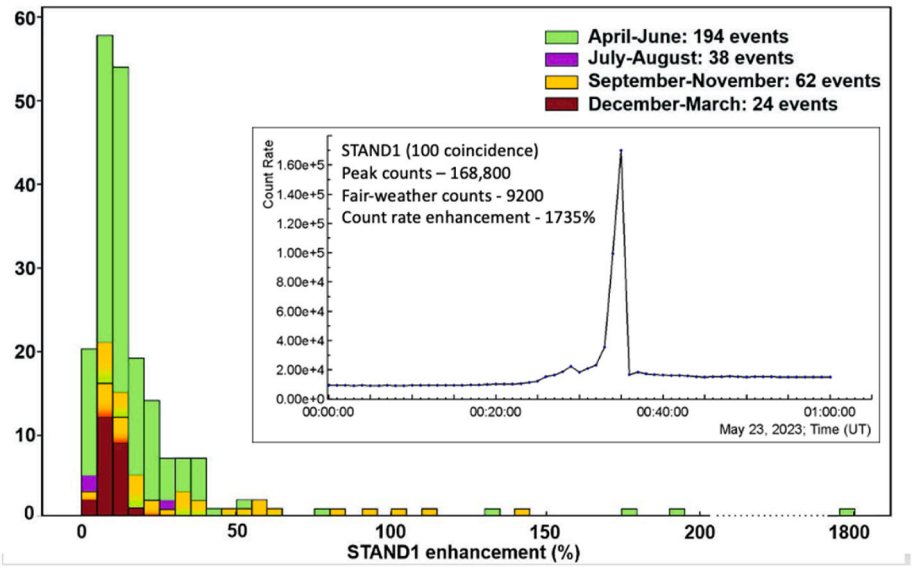

Fig. 4. The season-dependent histogram of TGE enhancements in percent. The 1 cm thick and 1 m^2 area plastic scintillator of the STAND1 detector was used for the relative enhancement calculation. In the inset, we show the 1-min time series of this scintillator count rates and the significance of the peak.

a particle avalanche. We accept the tripole model of the electrostatic field of a thunderstorm according to J. Kuettner's measurements at the Zugspitze in 1945-1949 [24]. NSEF during thunderstorms on Aragats varies from −30 – +20 kV/m, and the intracloud electric field sometimes exceeds 2.1 kV/cm (not a direct measurement, an estimate using the recovered energy spectra), prolonging almost to the Earth's surface.

In Fig. 4, the histogram of the TGE occurrences is ranged according to the percent of the flux enhancement. For comparative purposes, the four seasons are presented in different colors. The histogram showed 318 TGE events from 11 years (2013-2023) when the electric field sensors and weather stations were installed on Aragats. In 2008-2012, 277 TGE events were observed; however, meteorological and electricity sensors were not installed. Thus, the total number of TGE events surpasses 600. The TGEs were selected if three independent particle detectors demonstrate simultaneous peaks in the count rate time series larger than three sigma and the NSEF absolute value exceeds five kV/m.

On the right side of Fig. 4, we show the enhancement counting 1735 % of an extraordinarily large TGE that occurred on 23 May 2023. While such outliers are expected in an infinite number of measurements, it is unlikely to obtain such a huge TGE in only 318 trials.

Figs. 5–7 provide detailed information on TGE development measured by the STAND1 detector near the GAMMA surface array. We demonstrate count rates of 1-cm thick upper and stand-alone 3-cm thick scintillators. The energy threshold of 1 cm thick scintillator is lower than 3 cm thick; thus, its count rate is higher. The STAND1 unit near the SKL hall was buried in heavy, wet snow, causing TGE particle absorption. As we see in the Figures, the count rate was rather stable at the minute of maximum flux, Fig. 6a (1-s time series) and Fig. 7a (50-ms time series). In Fig. 6b and 7b, we show the count rate mean values and variances before TGE at fair weather at the same time one day before. As we see from the figures, during TGE the count rate enhanced more than ten times. The TGE significance recalculated for a minute time series (a

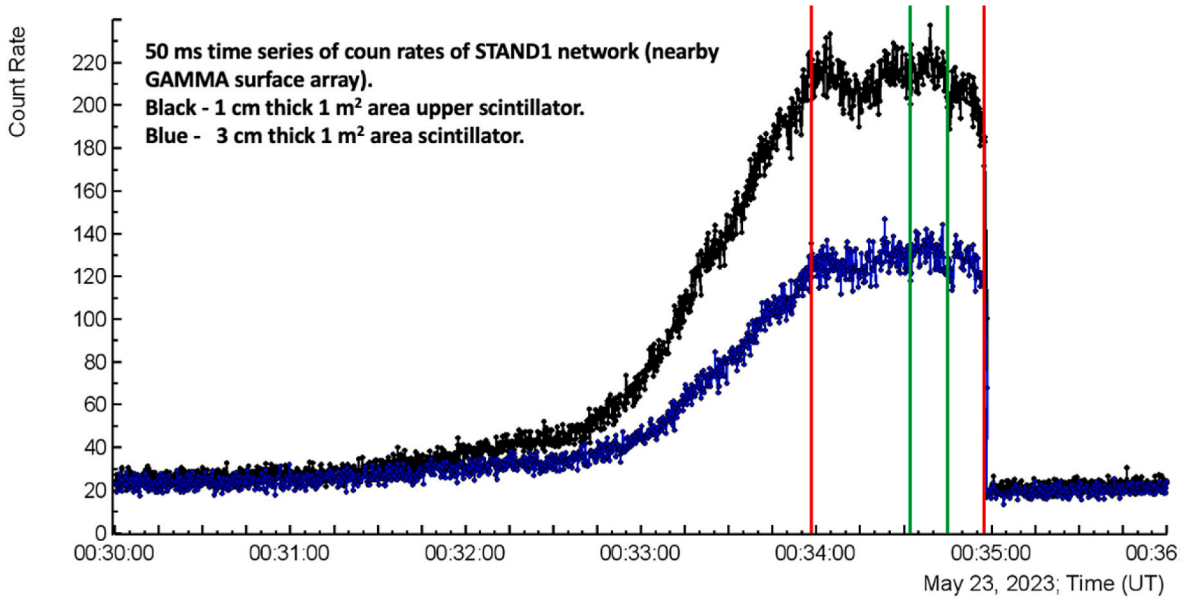

Fig. 5. Development of 23 May TGE. By the red lines, we show the maximum flux minute of TGE, and by the green lines – the maximum flux is 10 s. (For interpretation of the references to color in this figure legend, the reader is referred to the Web version of this article.)

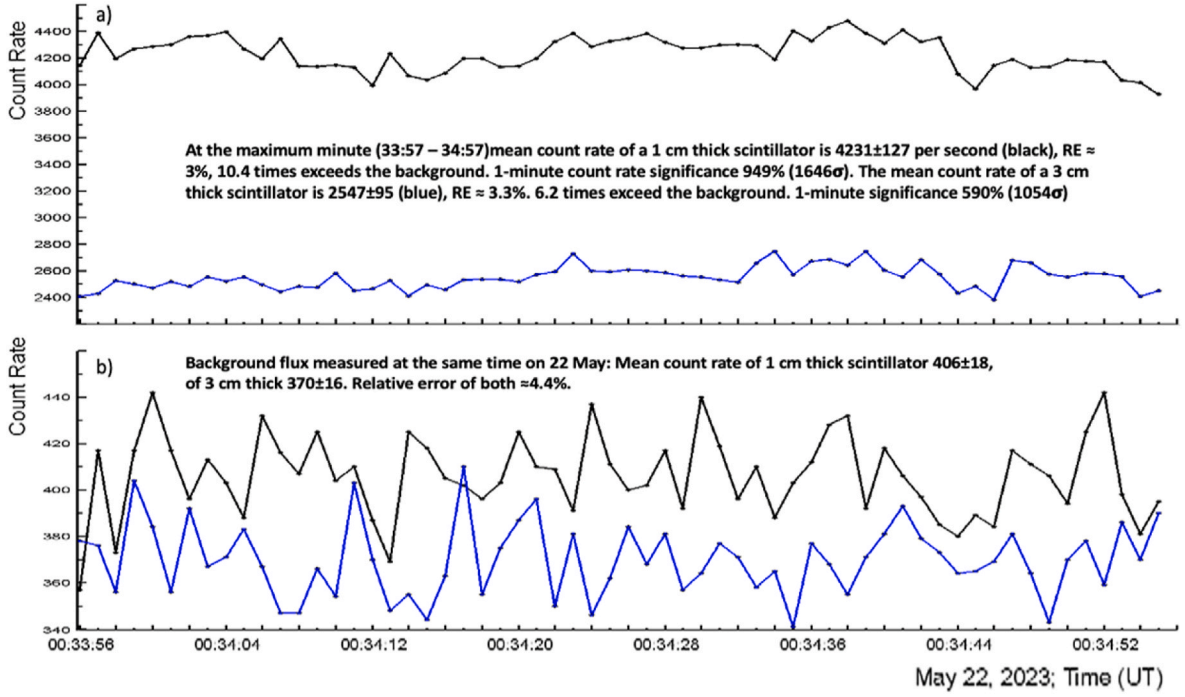

Fig. 6. a) - the maximum minute of the TGE, b) – the background count rate.

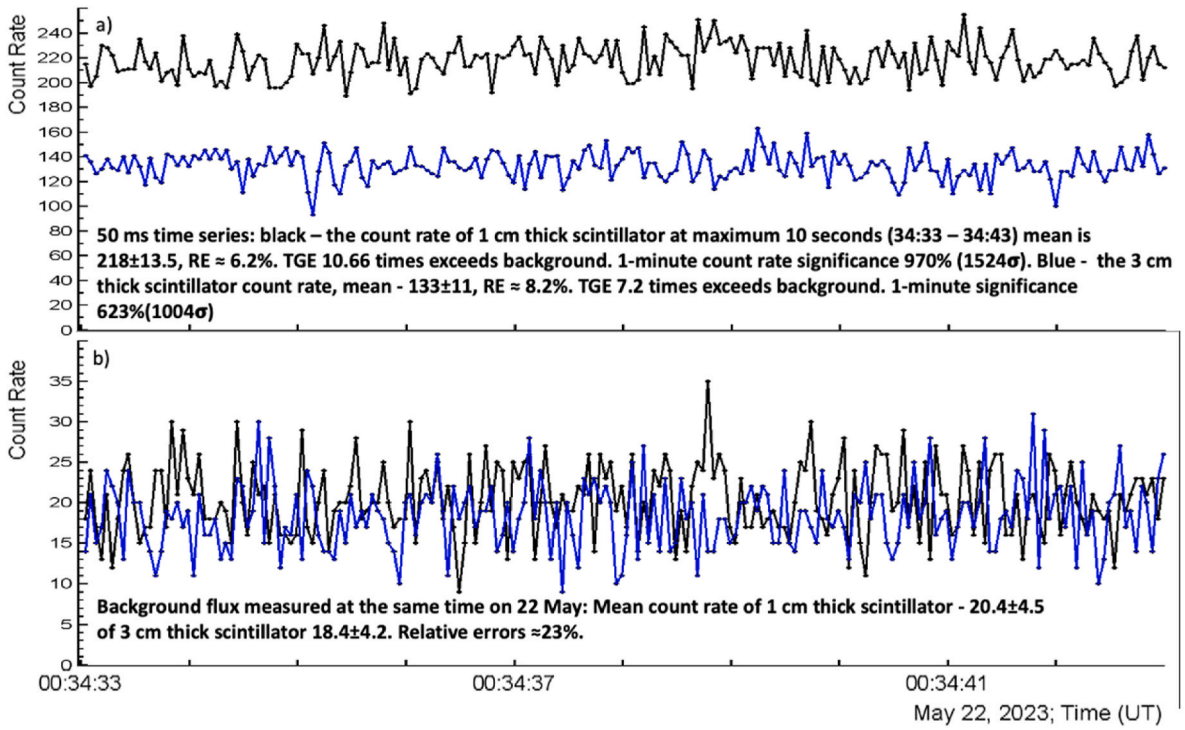

Fig. 7. a) time series of the maximum 10 s of TGE, b) background count rates.

standard adopted for the TGE comparisons) for the 1 cm thick scintillator reaches ≈1000 % and ≈1500 standard deviations from the background mean value. The relative enhancement measured with the upper scintillator of the STAND1 detector located near the GAMMA array was smaller compared to the one shown in Fig. 4. This is because the relative enhancement shown in Fig. 4 was obtained with "100″ coincidence, which selected low-energy particles resulting in larger enhancements compared to the ones obtained with all particles (Figs. 6 and 7). The relative errors (REs) of the count rates at TGE time and fair weather were 3 % and 4.4 %, respectively. Thus, the TGE particle flux was more stable than the ambivalent cosmic ray flux observed during fair weather. The same behavior is found for the 3 cm thick scintillator and the 50 ms time series.

4. Digitization of particle signals from the fast oscilloscope

The digitizing oscilloscope sampling rate of 6.4 ns is smaller than the particle pulse full width on a half maximum (FWHM) of 25–35 ns. For outlining particle pulses, we calculate the curves' derivatives obtained from the sequence of sampling amplitudes. When the derivative sign changes from negative to positive and the amplitude is lower than −32 mV, we consider the sampling time as a particle arrival. If we look only at amplitudes, we will count five particles below the threshold of −32 mV (crosses below the red line in Fig. 8); however, there is only one!

Fig. 9 presents distributions of pulse amplitudes measured during TGE and at fair weather, 100 ms before trigger at 00:33:52.9 and 100 ms after trigger (the same sample for the fair weather). In the 3,125 million sampling intervals, 331 particles were selected during TGE and 123 particles at fair weather (CUBE's N2 scintillator attached to oscilloscope's channel A). The difference is 208 for 200 ms, i.e., expected 1040 for 1 s.

The tradeoff between suppressing the PM noise and obtaining high signal detection efficiency leads to setting the threshold of the input signal stream to −32 mV. However, we have to check if the count rate is not suppressed by choosing this threshold. As we can see from Fig. 2, the three CUBE scintillators (N 2,3,6) are attached directly to the oscilloscope. To calibrate the intensity measured by the oscilloscope, we use the same type of detector, CUBE's N 1 scintillator, attached to a scaler that counts the number of particles per minute. Both detectors are located nearby on the floor of the SKL hall, see Fig. 3. Fig. 11 shows the 1-min count rate of the CUBE's scintillator N1 during TGE. At the maximum minute of TGE, the count rate was 102,500. The difference with fair weather count is 69,000, which makes 1150 per second. It is rather close to the number expected for the CUBEs' second detector – 1040. In the inset to Fig. 10, we see that CUBE's 2,3,6 scintillators' 1-s count rates (recalculated from 200 ms counts) are very close. The mean 1-s count of 2,3,6 scintillators rate makes 1170, which is close to 1150 directly measured by the CUBE's scintillator N1 at maximum TGE flux. Slightly different efficiencies of scintillators can explain the small in-channel differences.

The pulses from the outdoor 3-cm thick scintillator near the MAKET experimental hall are larger; see Fig. 11, a, b, c, and d. Also, we detect double-pulsed patterns (see Fig. 12). To avoid double counting, we set an artificial "dead-time" of 1μs, within which we do not accept any additional signals.

Fig. 13 shows the oscilloscope particle registration at TGE maximum flux and at fair weather. The TGE count rate outperforms the fair-weather count rate more than ten times, in good agreement with data shown in Figs. 5–7, measured by the STAND1 detector near the GAMMA surface array, 250 m apart from the unit located near the MAKET experimental hall. The large negative peaks (below −300 mV) are caused by either large energy particles or by the simultaneous registration of several particles from the tails of extensive air showers (EASs) hitting the detector.

5. Distribution of successive signals in the SKL and MAKET time series and correlation analysis of SKL signals

The distribution of registered particles' arrival times can reveal TGE's temporal structure. When a single seed electron initiates a large avalanche, it can alter the temporal pattern of particle arrivals, resulting in a distribution that differs from the expected Poisson distribution. To identify significant differences, we compare the number of particles registered within a time interval ΔT with the same number obtained from samples generated by the Poisson distribution. We use the mean value from 10 independent samples generated from the Poisson distribution. We also use the data obtained during fair weather conditions. In the second column of Table 1, we provide the intensity (number of particles per second) of the flux, recalculated from the 200 ms counts. In the third column, we present the time window. The fourth column lists the number of events falling within this window, and the fifth column displays the same number obtained with modeled Poisson variables. The right side of the Table shows the same parameters but obtained in fair weather.

As indicated in the table, there are differences between the expected Poisson values and the actual measurements in small time intervals,

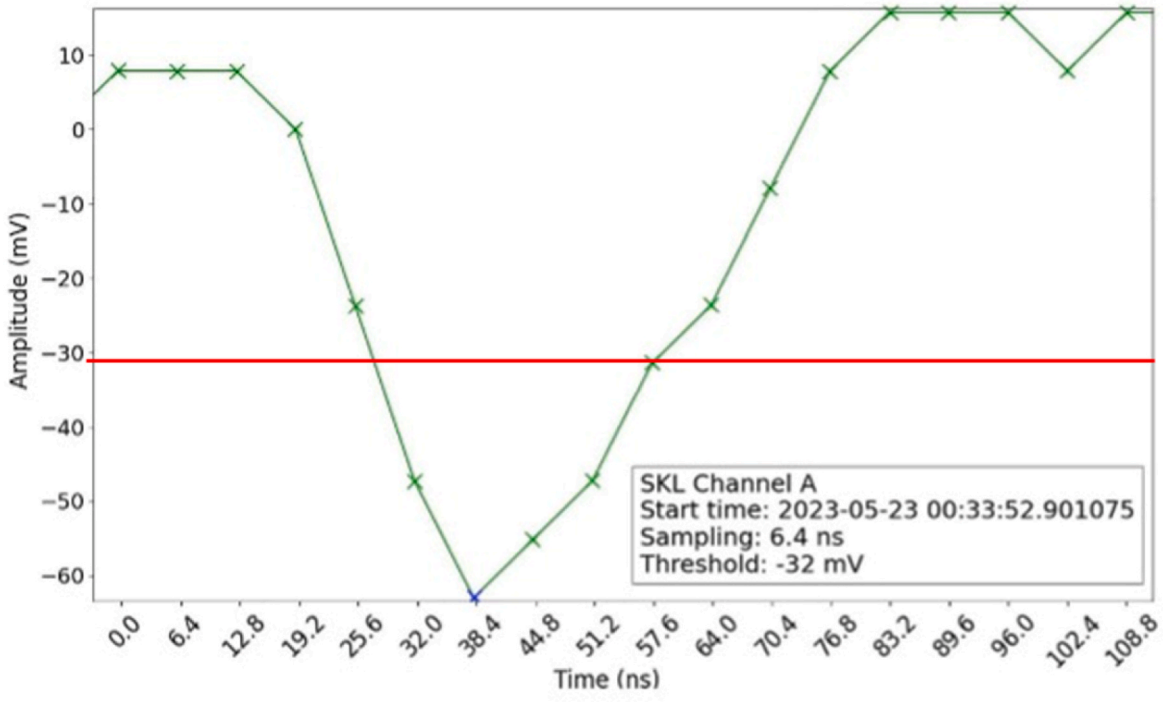

Fig. 8. The shape of the pulse as the oscilloscope enumerates it. The pulse is distributed among several bins of 6.4 ns each, shown as crosses. The red line shows the pulse amplitudes below the threshold of 32 mV. The full width on a half maximum of the pulse is ∼ 30 ns.

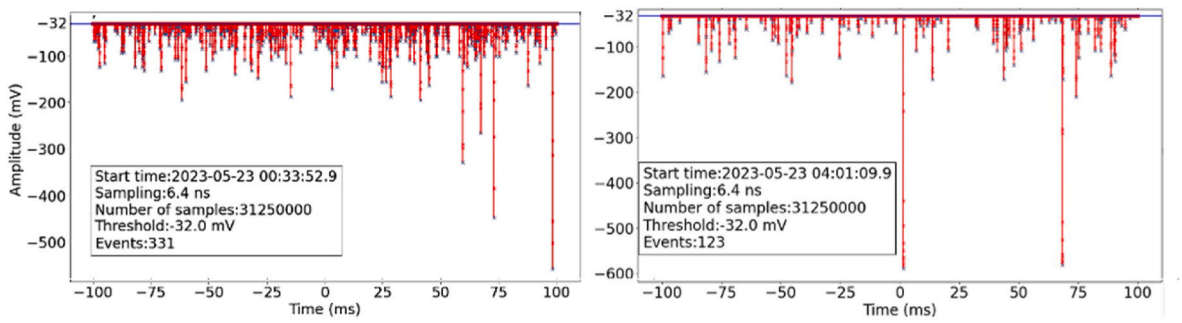

Fig. 9. a) signals registered by the digital oscilloscope (channel A, CUBE scintillator N 2). The oscillogram contains data for 200 ms, 100 ms before trigger, and 100 ms after trigger that occurred at 00:33:53 UT on May 23, 2023, frame, and at 04:10 the same day, frame b). In the insets, we show signal sampling information and the number of selected events.

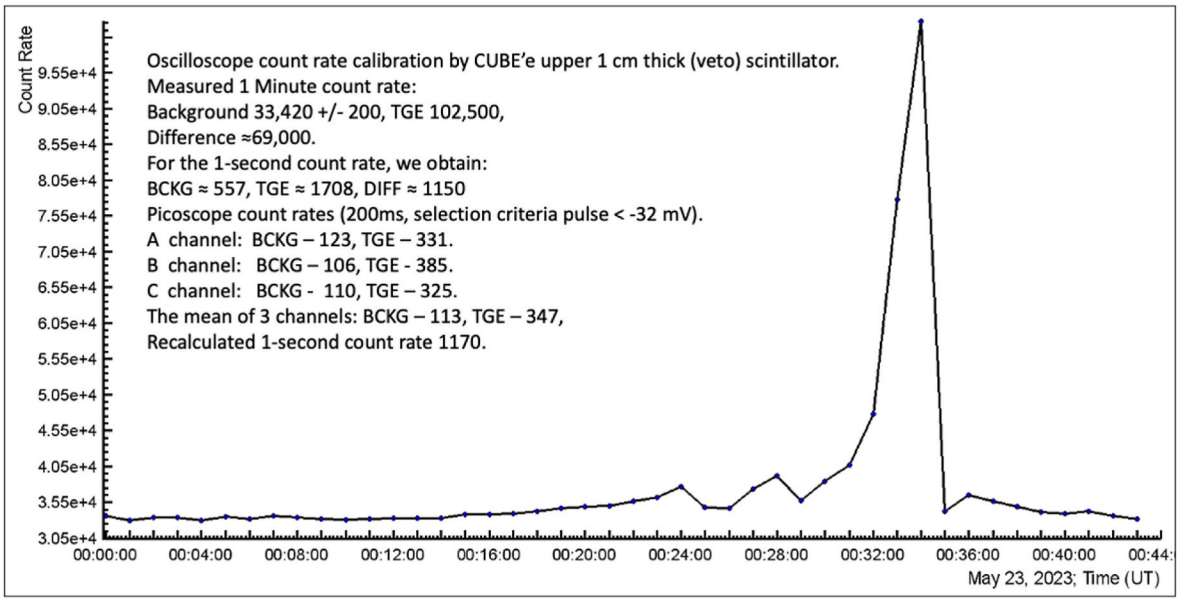

Fig. 10. Time series of 1-min count rate of 1 cm thick plastic scintillator CUBE's N 1. The inset compares 200 ms count rates of the A, B, and C oscilloscope channels (CUBE 2,3,6) with CUBE's N1 scintillator.

particularly in channels B and C. These deviations could be attributed to avalanche particles with minimal time separation. However, it is also possible that the tails of extensive air showers cause the arrival of time-tight events. Furthermore, we observe a significant discrepancy in channel C during fair weather conditions. No significant differences exist in the experimentally measured distances between successive events and Poison generated samples for the large time windows from 100 to 500 μs

Table 2 compares the inter-channel correlations with the expected Poisson values. To do this, we again generated ten independent samples following the Poisson distribution. We compared the mean number of events within time windows ranging from 320 ns to 640 μs to the measured values. We found discrepancies in the correlations between A and B channels at smaller time windows. However, the other two correlations did not show any significant differences.

Thus, Tables 1 and 2 can't reveal particle grouping in shorter subsamples despite some discrepancies from the Poisson distribution.

Fig. 14a shows the extended to 200 ms time series of the STAND1's TGE detection. Fig. 14b shows a time series obtained with randomly generated 992 events (the same number of events as measured by MAKET's STAND1 detector) from the Poisson distribution. The simulation aims to demonstrate that TGE particles come randomly as a mixture of multiple avalanches developed in the large-scale thunderous atmosphere.

To prove that the arrival time of TGE particles follows exponential interarrival time distribution (directly connected to Poisson distribution), we conducted a Kolmogorov-Smirnov (KS) test to compare a sample distribution with a reference probability distribution. Our approach involved generating 100 independent samples, each containing 992 timestamps, distributed according to Poisson distribution within a 200 ms interval. Fig. 15 displays the histogram of pairwise comparisons of the MAKET data at 00:34:52.9 with each of 100 generated Poisson-distributed samples.

The mean value of the KS test averaged by 100 values was 0.036, corresponding P-value of 0.544. Based on the high P-value of the KS statistics, it is evident that TGE particle arrivals occur independently of one another on May 23, 2023, and the time intervals between their arrivals follow a Poisson process.

6. Comparison of thunderstorm ground enhancements (TGEs) and terrestrial gamma-ray flashes (TGFs)

Several models aimed to explain the intensity of TGFs measured at 400–600 km from the source by the orbiting gamma detectors. The TGF source has mostly been characterized by three observables: fluence, source altitude, and beam opening angle. The number of electrons at the TGF source is estimated at around 10^{17}, assuming a source altitude of 15 km [25]. However, the seed electrons from the ambient population of

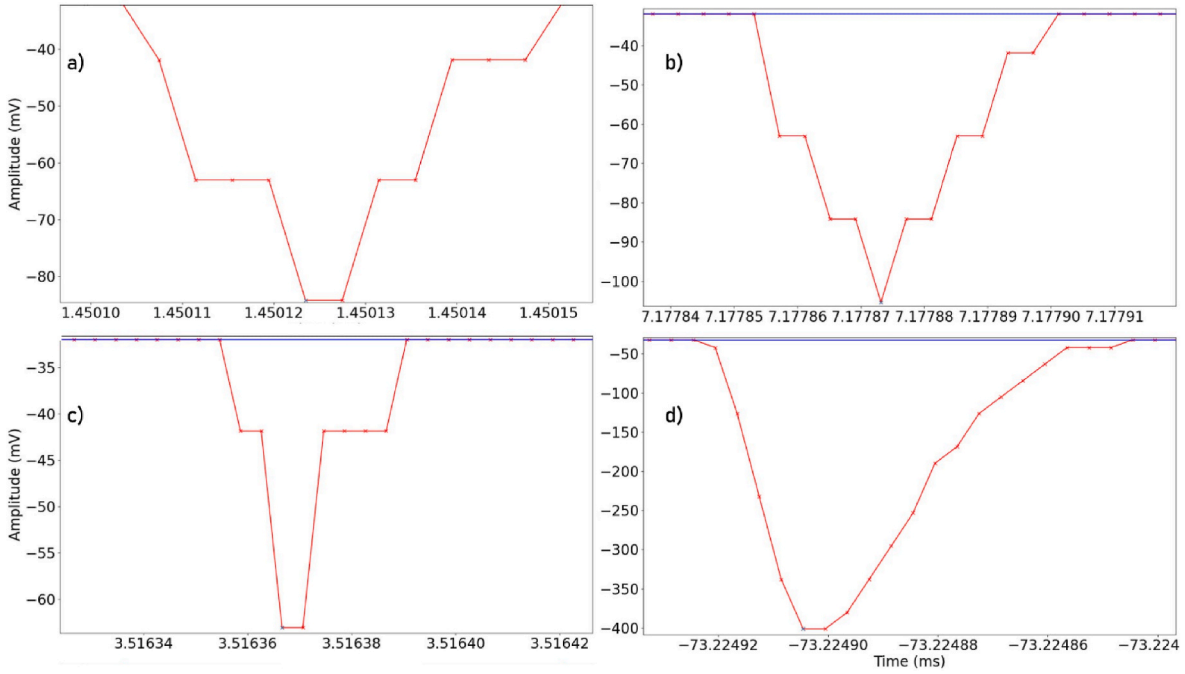

Fig. 11. Different shapes of the signals from the 3 cm thick scintillator digitized by the oscilloscope, sampling time four ns.

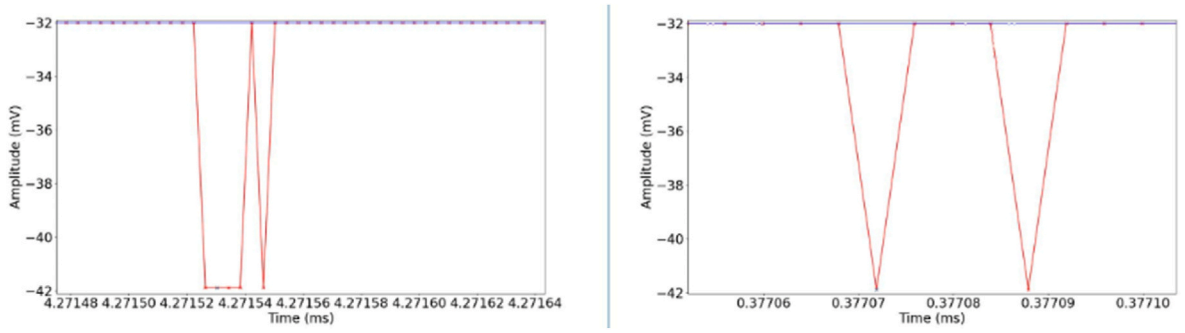

Fig. 12. Neighboring pulses will be counted as two particles; we introduce a "dead time" of 1 μs to avoid double counting.

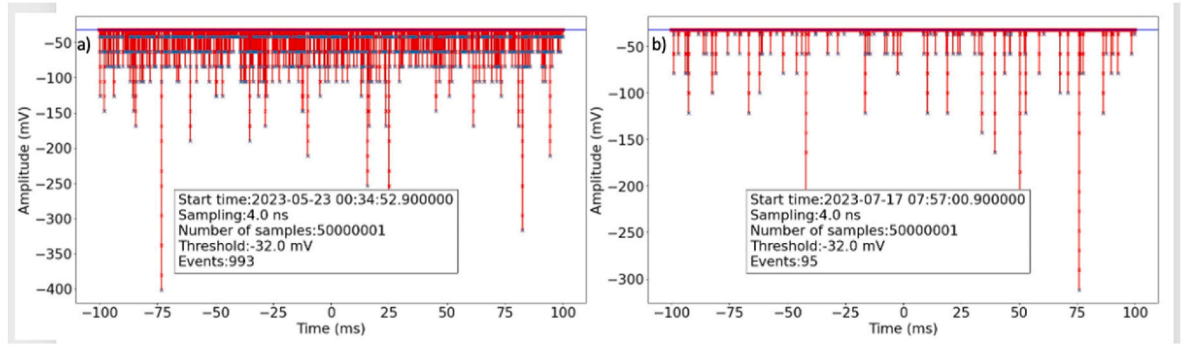

Fig. 13. a) signals registered by the digital oscilloscope (MAKET's channel B, 3 cm thick stand-alone outdoor scintillator). The oscillogram contains data for 200 ms, 100 ms before trigger, and 100 ms after trigger that occurred at 00:34:52.9 UT on May 23, 2023; b) the same at 07:57:01 on July 17, 2023. In the insets, we show signal sampling information and the number of selected events.

cosmic rays alone cannot account for this number. Two hypotheses have been proposed to explain this discrepancy: the relativistic feedback mechanism [5] and the thermal runaway mechanism [26]. In the relativistic feedback mechanism, positrons born in RREA accelerate in a direction opposite to electrons. Backscattered gamma rays returning to the "source" point produce electron-positron pairs. These two processes greatly enlarge the number of seed electrons, producing multiple RREAs and multiplying the number of seed electrons in the atmosphere. On the other hand, in the thermal runaway (cold runaway) mechanism, numerous seed electrons are produced in the high electric field in front

Table 1
Comparison of observed time between successive events (fallen within a chosen period) with expected from the Poisson distribution for the TGE and fair weather.

TGE: SKL (A, B, C channels) and MAKET (2 triggers, B channel)					Fairweather (same channels as for TGE)			
	I_0	ΔT (μs)	Events in ΔT	Poisson events in ΔT	I_0	ΔT (μs)	Events in ΔT	Poisson events in ΔT
Channel A	**1655**	**0–10**	**7**	**5 ± 2.2**	**615**	**0–10**	**1**	**0.75 ± 0.87**
		10–100	**42**	**45 ± 6.7**		**10–100**	**6**	**6.5 ± 2.6**
		100–500	**146**	**136 ± 11.7**		**100–500**	**23**	**25 ± 5**
Channel B	**1925**	***0–10***	***15***	***7 ± 2.6***	**530**	**0–10**	**0**	**0.56 ± 0.76**
		10–100	***36***	***60 ± 7.7***		**10–100**	**4**	**4.8 ± 2.2**
		100–500	**181**	**170 ± 13**		**100–500**	**23**	**19 ± 4.3**
Channel C	**1625**	***0–10***	***11***	***5 ± 2.2***	**550**	**0–10**	***6***	***0.66 ± 0.78***
		10–100	***34***	***43 ± 6.6***		**10–100**	***9***	***5.3 ± 2.3***
		100–500	**134**	**131 ± 11.4**		**100–500**	**25**	**21 ± 5**
MAKET	**3020**	**1–10**	**15**	**18 ± 4.2**	**475**	**0–10**	**2**	**0.44 ± 0.66**
		10–100	**151**	**139 ± 11.8**		**10–100**	**3**	**4 ± 2**
		100–500	**292**	**312 ± 17.7**		**100–500**	**16**	**15.6 ± 4**
MAKET	**4960**	**1–10**	**35**	**48 ± 6.9**	**475**	**0–10**	**2**	**0.44 ± 0.66**
		10–100	**342**	**340 ± 18.4**		**10–100**	**3**	**4 ± 2**
		100–500	**540**	**521 ± 22.8**		**100–500**	**16**	**15.6 ± 4**

Table 2
The correlation analysis of registered signals from SKL plastic scintillators.

Coincidences SKL	I_0	ΔT (μs)	Number of coincidences (Poison) in ΔT	Number of coincidences SKL A B C
AB	**1655**	**0.32**	***1.0***	***5***
	1925	**0.64**	***2.0***	***15***
		1.28	***4.4***	***20***
		6.4	**20.1**	**20**
		12.8	**39.9**	**45**
		128	**402.7**	**390**
		640	**2027.0**	**2055**
AC	**1655**	**0.32**	**0.9**	**0**
	1625	**0.64**	**1.8**	**5**
		1.28	**3.5**	**5**
		6.4	**17.3**	**15**
		12.8	**34.7**	**30**
		128	**339.9**	**325**
		640	**1719.6**	**1760**
BC	**1925**	**0.32**	**1.1**	**0**
	1625	**0.64**	**1.9**	**0**
		1.28	**3.9**	**0**
		6.4	**20.6**	**15**
		12.8	**39.1**	**50**
		128	**400.5**	**365**
		640	**2004.3**	**2020**

of streamers near the lightning.

Orbiting gamma detectors are not designed to handle gamma rays coming from the Earth's direction. The offline triggers select TGF gamma rays with low efficiency due to the lengthy dead times of electronics. Thus, the few detected gamma rays in each TGF allow only cumulative energy spectra to be recovered. However, mechanically combining gamma rays from different TGFs fails to capture crucial spectral diversity, making it impossible to select the best model.

The energy spectra of 46 TGFs detected by Fermi-GBM were compared to Monte Carlo simulations of the RREA model. This model included the propagation of the RREA particles through the atmosphere using narrow- and wide-beam options [27]. The TGF sample had between 21 and 53 counts per TGF in one Bismuth Germanate scintillator (BGO). According to the narrow beam model, the bremsstrahlung photons are distributed within the RREA region. In the wide-beam model, the photons are emitted isotropically in a cone with a half opening of 45°. However, due to the small size of TGFs and instrumental drawbacks, it was impossible to differentiate between the narrow- and wide-beam models.

Fortunately, the Atmosphere-Space Interactions Monitor (ASIM, [28]) on board the International Space Station observed a vast amount of statistically provided TGFs. ASIM detector is much more efficient in registering TGFs than other orbiting gamma detectors designed to detect gamma rays from violent explosions in the Universe, which use complicated off-line triggers to find TGFs from the Earth's direction. The High-Energy Detector (HED) of an area of 900 cm^2 detects gamma rays with energies ranging from 0.3 to 30 MeV with 30 ns resolution. HED data stream is synchronized with optical imaging of atmospheric discharges using photometers that operate in UV, blue, and red bandwidths with a sampling rate of 100 kHz. The device also features two optical

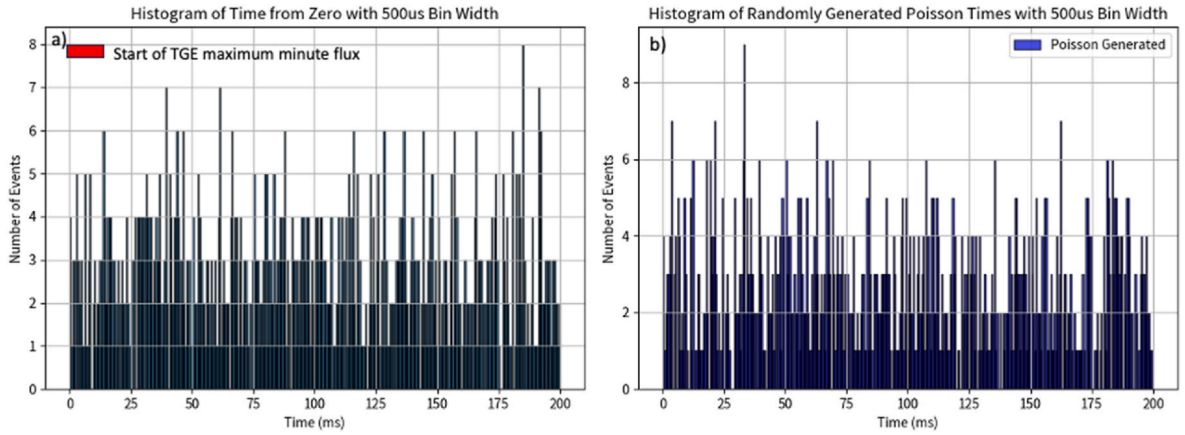

Fig. 14. a) 200 ms time series of the TGE particle arrival times registered by STAND1 detector near MAKET experimental hall; zero time corresponds to 00:34:52.9 on May 23, 2023. b) time series of the Poisson random times within 200 ms. The bin width of both is 500 μs

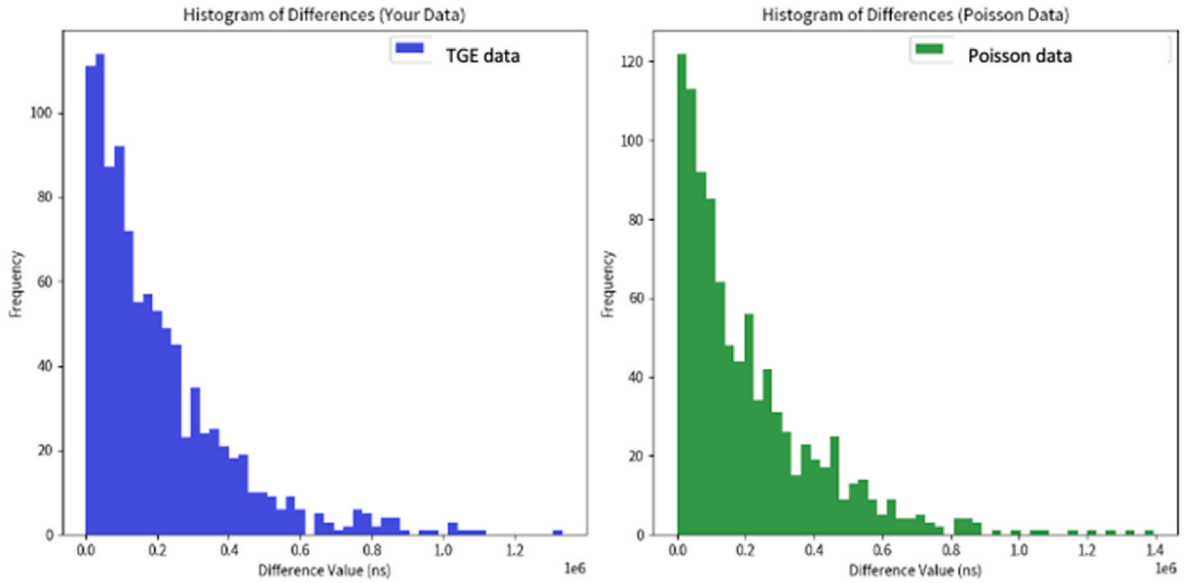

Fig. 15. Histogram of the KS test statistics for pair-wise comparison of MAKET and 100 Poisson distributed samples.

cameras that capture up to 12 frames per second and operate in the 337 and 777 nm bandwidths. Based on the analysis of 17 ASIM TGFs, it was confirmed that the source's brightness varies significantly. The number of photons with energies greater than 1 MeV ranged from 10^{16} to 10^{20} [29]. However, the same publication admitted that for "instruments with effective areas in the range of a few hundred cm^2, it is very difficult to constrain reliably the source properties without the help of simultaneous measurements in the radio band".

Nonetheless, ASIM is the only detector specifically designed for TGF detection, and it has already measured prolonged gamma-ray bursts from RREAs following one another within a time window of up to 10 ms [30]. This allows for directly comparing the millisecond time series of TGEs and TGFs. In Fig. 16, we compare the 10 ms duration time series of the multi-pulse TGF [30], registered by ASIM, and the same duration time series from the STAND1 detector. The difference between TGFs, which last for milliseconds, and TGEs, which last for minutes, is not due to different origination mechanisms but different experimental arrangements. The RREA avalanches go out from thundercloud on Aragats usually 50–150 m above the Earth's surface. It allows the registration of millions of TGE particles and reliable recovery of electron and gamma-ray energy spectra with spectrometers with an area of tens of m^2. Thus, the distance from the source to the detector in TGE measurements is 1000 times less than in TGF measurements. The number of particles for large TGEs is ~ 10,000 times larger than TGFs. The area covered by particle detectors is a million times larger in TGE research compared with TGF. The crucial evidence for RREA research, namely electron energy spectra, is also possible from registered TGEs, and not for TGFs. Fig. 16a shows an intense gamma-ray burst followed by a few discrepant gamma rays registered by ASIM's HED detector (refer to Fig. 6.1 in Ref. [30]). Fig. 16b shows a more-or-less uniform distribution of particles registered by the STAND1's plastic scintillator. On Aragats, RREAs produce a very stable flow of particles for many seconds due to the proximity to the source (Fig. 6). Only the most energetic gamma rays from RREAs can reach the Space Station 400 km from Earth, producing a short particle burst. Nonetheless, despite their difference, TGFs and TGEs share many similarities in their origin. If large particle detectors placed on balloons or aircraft fly at 15–20 km altitude, they can also detect millions of TGF particles resulting from intense RREAs in the upper dipole.

In Fig. 17, we demonstrate the uniformity of particle arrival over 200 ms of recorded time series. The frames (a-d) show successive 10 ms long time series of 50 registered particles with ordered numbers from 700 to 900. These time series do not show bursts that could be attributed to a very energetic particle avalanche occasionally captured by the detector.

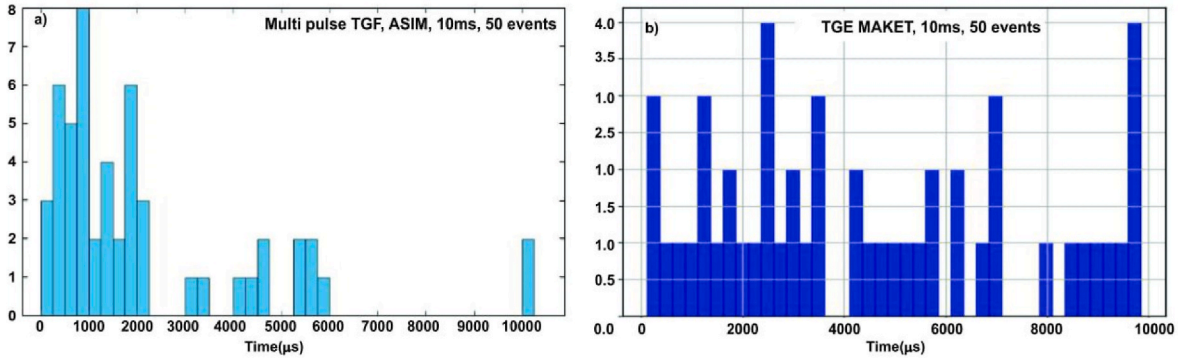

Fig. 16. a) Time series of gamma-ray arrival times from the onset of the first TGF until the onset of the last TGF, registered by ASIM's high-energy detector (HED) detector; b) Time series of the TGE particle arrival times registered by STAND1 detector near MAKET experimental hall; zero time corresponds to 00:34:53.1 on May 23, 2023. The bin width of both is 250 μs

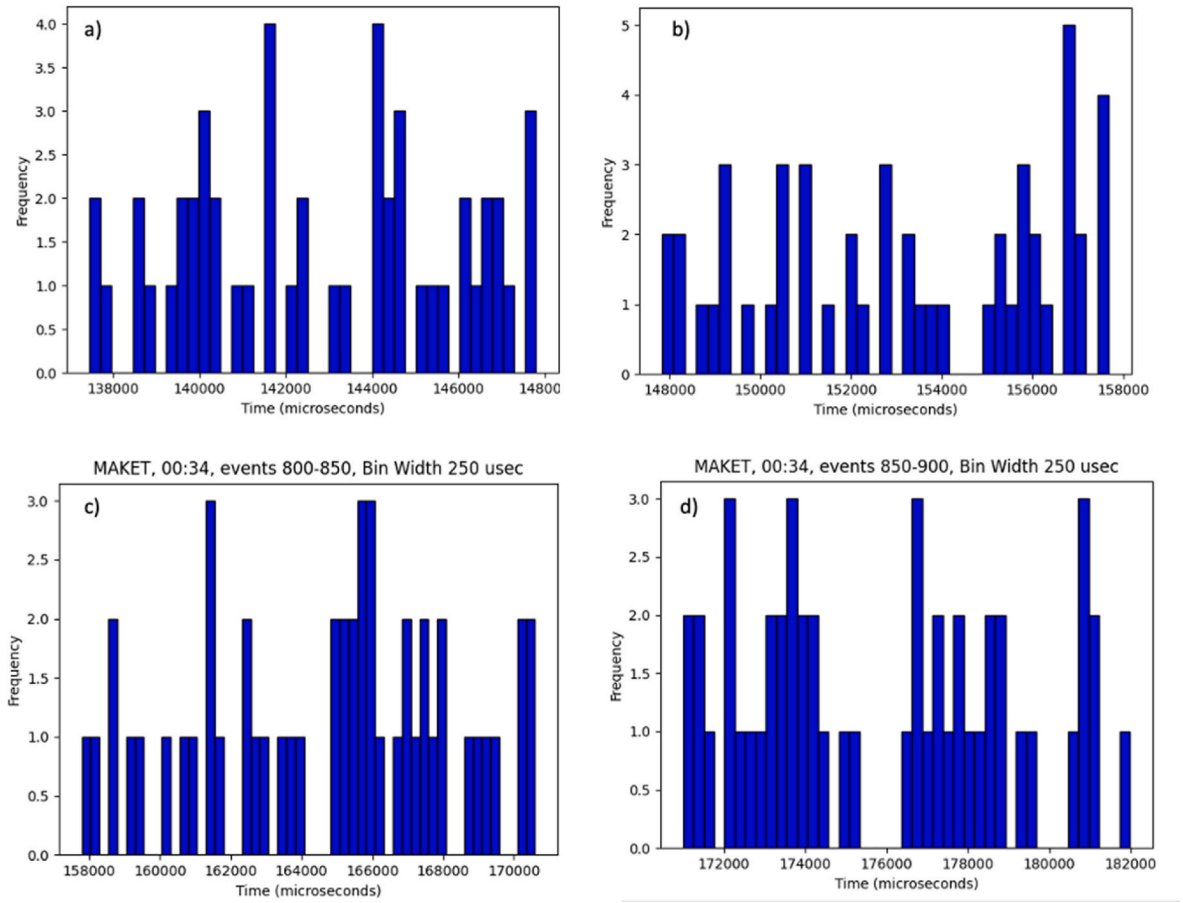

Fig. 17. Successive 10 ms time series of TGE particle detection by 3-cm thick scintillator attached to digitizing oscilloscope.

7. CORSIKA simulation of TGE particle arrival times and distances

To get insight into the expected space-temporal distributions of the RREA particles, we perform a simulation study with the CORSIKA code [31] version 7.7400, which considers the electric field's effect on the particles' transport. We use electrons with energy 1 MeV as seed particles; the electric field was introduced at 5200 m in a strong electric field of 2.1 kV/m. Thus, the strength of the electric field is ~ 25 % higher than the critical strength at 4000–5000 m heights. We store arrival times and radial distances of all RREA electrons reaching the ground level of 3200 m from 1000 simulation trials. The propagation of electrons and gamma rays was followed in the avalanche until their energy decreased to 0.05 MeV. As illustrated in Fig. 18a, the mean arrival time of RREA electrons is within ≈7.5 μs (FLHM). For radial distances shorter than 10 m, the RREA collection time is even smaller - ≈150 ns (Fig. 18b).

A large number of secondary electrons and gamma rays are produced in the atmospheric electric field and arrive at the Earth's surface in a very short time. Although the seed electrons are injected into the electric field from the same point, the radial distribution is quite dispersed. Only about 3 % of the electrons fall within a circle with a radius of 10 m around the injection point projected onto the ground. Thus, multiple RREAs from a large atmospheric volume above detectors create a uniform flow of TGE particles.

8. Conclusions

We perform a space-temporal analysis of the RREA process within the thunderous atmosphere. This analysis is based on detecting a large TGE on May 23, 2023, by a STAND1 network of particle detectors covering an area of 50,000 m^2. Our survey of the largest TGE includes a comprehensive statistical analysis of count rate time series ranging from nanoseconds to seconds (Figs. 5–7). The flux of RREA particles arrives at the Earth's surface independently and uniformly during many seconds enhancing the fair-weather flux more than ten times. Statistical analyses (Tables 1 and 2, Figs. 14 and 15) of particle arrival times and spatial

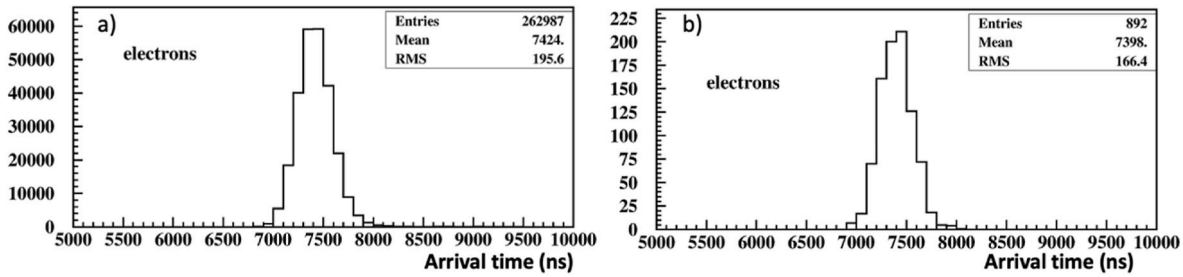

Fig. 18. The *arrival time* distribution of *electrons* total a) and a subsample in 10 m radii *b*).

correlations do not provide evidence for detecting separate ECSs (microbursts). Instead, the TGE is made up of a mixture of millions of RREAs that are created in vast atmospheric electric fields. The information about their source, which comes from a single seed electron at a certain altitude, is entirely blurred due to the large spatial dispersion of millions of secondary particles. The simulation study confirms our conclusion. The distribution of particles over several square kilometers results in particle densities of about 0.5 per square centimeter per second. Thus, electron accelerators operated in thunderclouds provide minutes-long steady flux of electrons and gamma rays covering multi km^2 areas on the Earth's surface.

To sum up, the RREA in the thundercloud above Aragats produced on 23 May 2023 a stable ten times higher particle flux than the fair weather ambient cosmic ray flux. The count rate of TGEs shows a smaller relative error when compared to the flux of the ambient population of cosmic rays during fair weather. TGE particles arrive uniformly and randomly, according to the Poisson process.

CRediT authorship contribution statement

A. Chilingarian: Writing – review & editing, Writing – original draft, Visualization, Validation, Supervision, Software, Resources, Project administration, Methodology, Investigation, Funding acquisition, Formal analysis, Conceptualization. **D. Pokhsraryan:** Validation, Software, Methodology, Formal analysis, Data curation. **F. Zagumennov:** Visualization, Software, Methodology. **M. Zazyan:** Visualization, Validation, Software, Methodology, Investigation.

Declaration of competing interest

The authors declare that they have no known competing financial interests or personal relationships that could have appeared to influence the work reported in this paper.

Data availability

Data will be made available on request.

Acknowledgments

The authors thank the Aragats Space Environmental Center staff for ensuring the uninterrupted operation of particle detectors and field meters. We would also like to thank Y. Khanikyanc for maintaining the file recording infrastructure and S. Soghomonyan's valuable contributions to discussions in the early project stage. Additionally, A.C. would like to thank Davit Aslanyan for preparing Fig. 4 and Suren Chilingaryan for introducing modern AI systems. The authors acknowledge the support of the Science Committee of the Republic of Armenia (Research Project No. 21AG-1C012) in the modernization of the technical infrastructure of high-altitude stations.

References

[1] A. Chilingarian, A. Daryan, K. Arakelyan, et al., Ground-based observations of thunderstorm-correlated fluxes of high-energy electrons, gamma rays, and neutrons, Phys. Rev. D 82 (2010), 043009.
[2] A. Chilingarian, G. Hovsepyan, A. Hovhannisyan, Particle bursts from thunderclouds: natural particle accelerators above our heads, Phys. Rev. D 83 (2011), 062001.
[3] G.J. Fishman, P.N. Bhat, R. Mallozzi, et al., R., Discovery of intense gamma-ray flashes of atmospheric origin, Science 264 (5163) (1994) 1313, https://doi.org/10.1126/science.264.5163.1313.
[4] A.V. Gurevich, G. Milikh, R. Roussel-Dupre, Runaway electron mechanism of air breakdown and preconditioning during a thunderstorm, Phys. Lett. A 165 (1992) 463.
[5] J.R. Dwyer, A fundamental limit on electric fields in air, Geophys. Res. Lett. 30 (20) (2003) 2055, https://doi.org/10.1029/2003GL017781.
[6] L.P. Babich, I.M. Kutsyk, E.N. Donskoy, et al., Comparison of relativistic runaway electron avalanche rates obtained from Monte Carlo simulations and kinetic equation solution, IEEE Trans. Plasma Sci. 29 (3) (2001) 430–438, https://doi.org/10.1109/27.928940.
[7] V.V. Alexeenko, N.S. Khaerdinov, A.S. Lidvansky, et al., Transient variations of secondary cosmic rays due to atmospheric electric field and evidence for pre-lightning particle acceleration, Phys. Lett. 301 (2002) 299–306.
[8] R. Roussel-Dupré, E. Symbalisty, Y. Taranenko, V. Yukhimuk, J. Atmos. Sol. Terr. Phys. 60 (1998) 917–940.
[9] J.R. Dwyer, A fundamental limit on electric fields in air, Geophys. Res. Lett. 30 (2003) 2055.
[10] L.P. Babich, E.N. Donskoy, R.I. Il'kaev, I.M. Kutsyk, R.A. Roussel-Dupré, Plasma Phys. Rep. 30 (2004) 616–624.
[11] Ashot Chilingarian, Gagik Hovsepyan, Dataset for 16 Parameters of Ten Thunderstorm Ground Enhancements (TGEs) Allowing Recovery of Electron Energy Spectra and Estimation the Structure of the Electric Field above Earth's Surface, Mendeley Data, 2022, https://doi.org/10.17632/tvbn6wdf85.2 vol. 1.
[12] Ashot Chilingarian, Gagik Hovsepyan, Davit Aslanyan, Balabek Aslanyan, Tigran Karapetyan, "Catalog of Thunderstorm Ground Enhancements (TGEs) Observed at Aragats in 2013- 2021", Mendeley Data, 2022, p. V1, https://doi.org/10.17632/8gtdbch59z.1.
[13] http//(crd.yerphi/ADEI).
[14] A. Chilingarian, G. Hovsepyan, Y. Khanikyanc, A. Reymers, S. Soghomonyan, Lightning origination and thunderstorm ground enhancements terminated by the lightning flash, EPL 110 (2015), 49001.
[15] A. Chilingarian, S. Chilingaryan, T. Karapetyan, Lev Kozliner, Yeghia Khanikyants, Gagik Hovsepyan, David Pokhsraryan, Suren Soghomonyan, On the initiation of lightning in thunderclouds, Sci. Rep. 7 (2017), https://doi.org/10.1038/s41598-017-01288-0. Article number: 1371.
[16] A. Chilingarian, G. Hovsepyan, B. Mailyan, In situ measurements of the Runaway Breakdown (RB) on Aragats mountain, Nucl. Instrum. Methods Phys. Res. A 874 (2017) 19–27.
[17] A.V. Gurevich, K.P. Zybin, R.A. Roussel-Dupre, Lightning initiation by simultaneous runaway breakdown and cosmic ray showers, Phys. Lett. A 254 (1999) 79.
[18] A. Chilingarian, S. Soghomonyan, Y. Khanikyanc, D. Pokhsraryan, On the origin of particle fluxes from thunderclouds, Astropart. Phys. 105 (2019) 54.
[19] G.I. Britvich, S.K. Chernichenko, A.P. Chubenko, et al., The large scintillation charged particles detector of the Tien-Shan complex 'ATHLET, ' Nucl. Instrum. Meth- ods A 564 (1) (2006) 225–234, https://doi.org/10.1016/j.nima.2006.03.042.
[20] S. Chilingaryan, A. Beglarian, A. Kopmann, S. Vöcking, Advanced data extraction infrastructure: web based system for management of time series data, J. Phys. Conf. 219 (2010), 042034, https://doi.org/10.1088/1742-6596/219/4/042034.
[21] D. Pokhsraryan, Fast Data Acquisition system based on NI-myRIO board with GPS time stamping capabilities for atmospheric electricity research, in: Proceedings of TEPA Symposium, Nor Amberd, vol. 2015, Tigran Mets, Yerevan, 2016, p. 23.
[22] A. Chilingarian, T. Karapetyan, M. Zazyan, G. Hovsepyan, B. Sargsyan, N. Nikolova, H. Angelov, J. Chum, R. Langer, Maximum strength of the atmospheric electric field, Phys. Rev. D 103 (2021), 043021.
[23] R. Langer Chum, J. Baše, M. Kollárik, I. Strhárský, G. Diendorfer, J. Rusz, Significant enhancements of secondary cosmic rays and electric field at high mountain peak during thunderstorms, Earth Planets Space 72 (2020) 28.
[24] Kuettner, The electrical and meteorological conditions inside thunderclouds, J. Meteorol. 7 (1950) 322.
[25] J.R. Dwyer, D.M. Smith, A comparison between Monte Carlo simulations of runaway breakdown and terrestrial gamma-ray flash observations, Geophys. Res. Lett. 32 (22) (2005), https://doi.org/10.1029/2005GL023848.
[26] S. Celestin, V.P. Pasko, Energy and fluxes of thermal runaway electrons produced by the exponential growth of streamers during the step- ping of lightning leaders and in transient luminous events, J. Geophys. Res. 116 (A3) (2011), https://doi.org/10.1029/2010JA016260.
[27] B.G. Marilyn, W. Xu, S. Celestin, M.S. Briggs, J.R. Dwyer, E.S. Cramer, et al., Analysis of individual terrestrial gamma-ray flashes with lightning leader models and Fermi Gamma-ray Burst Monitor data, J. Geophys. Res.: Space Phys. 124 (8) (2019) 7170–7183, https://doi.org/10.1029/2019JA026912.
[28] C.A. Skeie, N. Østgaard, A. Mezentsev, I. Bjørge-Engeland, M. Marisaldi, N. Lehtinen, et al., The temporal relationship between terrestrial gamma-ray flashes and associated optical pulses from lightning, J. Geophys. Res. Atmos. 127 (2022), e2022JD037128, https://doi.org/10.1029/2022JD037128.
[29] A. Lindanger, M. Marisaldi, D. Sarria, N. Østgaard, N. Lehtinen, C.A. Skeie, et al., Spectral analysis of individual terrestrial gamma-ray flashes detected by ASIM, J. Geophys. Res. Atmos. 126 (2021), e2021JD035347, https://doi.org/10.1029/2021JD035347.
[30] A. N. Fuglestad, Multi Pulse Terrestrial Gamma-ray Flashes and optical pulses of lightning observed by ASIM, Master Thesis in Space Physics, University of Bergen. https://bora.uib.no/bora-xmlui/bitstream/handle/11250/3073302/Multi-Pulse-Terrestrial-Gamma-ray-Flashes-and-optical-pulses-of-lightning-observed-by-ASIM-print-version.pdf?sequence=3&isAllowed=y.
[31] D. Heck, J. Knapp, J.N. Capdevielle, G. Schatz, T. Thouw, Forschungszentrum, Karlsruhe, Report No. FZKA 6019, 1998. https://www.ikp.kit.edu/corsika/70.php.

Acronyms

ADEI: Advanced Data Extraction Infrastructure, a software tool designed for handling and analyzing large datasets
ASIM: The Atmosphere-Space Interactions Monitor (ASIM) on board the Space Station

HED: ASIM's high-energy detector
GCR: Galactic cosmic rays
HEPA: High-energy physics in the atmosphere
RREA: Relativistic runaway electron avalanche
TGE: Thunderstorm ground enhancement
NSEF: Near-surface electrical field
TGF: Terrestrial gamma flash
DTGF: Downward TGF
ECS: Extensive Cloud Shower a RREA unleashed by a single seed electron entering a strong intracloud electric field
BGO: Bismuth Germanate (Bi4Ge3O12) scintillation material
CORSIKA: COsmic Ray SImulations for KAscade, a code
BOLTEK: Company producing EFM-100 electric field sensor
ASNT: Aragats Solar Neutron Telescope
CUBE: Detector located at the Aragats Space Environmental Center (ASEC)
STAND1: Particle detector network on Aragats
FSDAQ: Fast synchronized data acquisition system
KS: The Kolmogorov-Smirnov test is used in statistics to compare a sample with a reference probability distribution
FWMH: Full width on half maximum
RE: Relative error is a measure of the accuracy of a measurement compared to the actual value
PicoScope: A range of oscilloscopes produced by Pico Technology
MAKET: Experimental Hall on Aragats
SKL: Experimental Hall on Aragats